



Nanofluid convective heat transfer in a parallel-disk system

Yu Feng, Clement Kleinstreuer*

Department of Mechanical and Aerospace Engineering, North Carolina State University, Raleigh, NC 27695-7910, USA

ARTICLE INFO

Article history:

Received 10 May 2010

Received in revised form 27 May 2010

Accepted 27 May 2010

Available online 17 July 2010

Keywords:

Nanofluid

Convective heat transfer

Impinging-jet

Parallel disk

Entropy generation

Wall temperature control

ABSTRACT

Inherently low thermal conductivities of basic fluids form a primary limitation in high-performance cooling which is an essential requirement for numerous thermal systems and micro-devices. Nanofluids, i.e., dilute suspensions of, say, metal-oxide nanoparticles in a liquid, are a new type of coolants with better heat transfer performances than their pure base fluids alone. Using a new, experimentally validated model for the thermal conductivity of nanofluids, numerical simulations have been executed for alumina-water nanofluid flow with heat transfer between parallel disks. The results indicate that, indeed, nanofluids are promising new coolants when compared to pure water. Specifically, smoother mixture flow fields and temperature distributions can be achieved. More importantly, given a realistic thermal load, the Nusselt number increases with higher nanoparticle volume fraction, smaller nanoparticle diameter, reduced disk-spacing, and, of course, larger inlet Reynolds number, expressed in a novel form as $Nu = Nu(Re \text{ and } Br)$. Fully-developed flow can be assumed after a critical radial distance, expressed in a correlation $Re_{crit} = fct(Re)$, has been reached and hence analytic solutions provide good approximations. Nanofluids reduce the system's total entropy generation rate while hardly increasing the required pumping power for any given Re_{in} . Specifically, minimization of total entropy generation allows for operational and geometric system-optimization in terms of $S_{gen} = fct(Re \text{ and } \delta)$.

© 2010 Elsevier Ltd. All rights reserved.

1. Introduction

For pure fluids, inherently low thermal conductivities form a primary limitation in high-performance cooling which is the essential requirement for numerous thermal systems and micro-devices. Nanofluids, i.e., dilute suspensions of, say, metal-oxide nanoparticles in a liquid, are a new type of coolants with better heat transfer performances than their pure base fluids alone. Specifically, numerous experiments with nanofluids have demonstrated thermal conductivity enhancement, indicating promising applications to micro-scale cooling. Compared to pure liquids, experimental evidence showed that the thermal conductivity of nanofluids, k_{nf} , significantly increases comparing at small nanoparticle volume fractions, with decreasing nanoparticle diameter and elevated mixture temperature. For example, Lee and Choi [1] investigated CuO-water/ethylene glycol nanofluids with particle diameters 18.6 and 23.6 nm as well as Al₂O₃-water/ethylene glycol nanofluids with particle diameter 24.4 and 38.4 nm and discovered a 20% thermal conductivity increase at a volume fraction of just 4%. Wang et al. [2] determined experimentally a 12% increase in k_{nf} with 28 nm-diameter Al₂O₃-water and 23 nm-diameter CuO-water nanofluids at 3% volume fraction. Eastman et al. [3] reported a 40% thermal conductivity increase for 10 nm-diameter

Cu-water nanofluids with a volume fraction of only 0.3%. Li and Peterson [4] provided the thermal conductivity expression in terms of temperature (T) and volume fraction (ϕ) by using curve-fitting for CuO-water and Al₂O₃-water nanofluids. Additionally, Xie et al. [5] investigated SiC-water nanofluids and Hong et al. [6] focused on Fe-water nanofluids. Recently, Chopkar et al. [7] investigated Ag₂Al-water nanofluids and Al₂Cu-water nanofluids and reported a 130% increase in thermal conductivity with a volume fraction less than 1%. Considering particle diameters of 47 and 36 nm, Mintsa et al. [8] provided new thermal conductivity expressions for Al₂O₃-water and CuO-water nanofluids. Murshed et al. [9] reported a 27% increase in 4% TiO₂-water nanofluids with a particle diameter of 15 nm and a 20% increase for Al₂O₃-water nanofluids. However, Duangthongsuk and Wongwaisaes [10] observed a more moderate increase for TiO₂-water nanofluids. Das et al. [11] commented systematically on the relationship between k_{nf} and temperature demonstrating that the thermal conductivity of nanofluids will significantly increase with higher temperatures. Patel et al. [12] confirmed the temperature effect obtained by Das et al. [11] as well as the findings of Lee et al. [1]. They also showed the inverse dependence of particle size on thermal conductivity enhancement, considering three sizes of alumina nanoparticles suspended in water.

Still, controversies for $k_{nf}(\phi, T)$ persist [13–18]. More recently, scientists used optical measurement methods [14–18] to obtain the effective thermal conductivities of nanofluids and found no anomalous increase, which brings the transient hot-wire (THW)

* Corresponding author. Tel.: +1 9195155261; fax: +1 9195157968.
E-mail address: ck@eos.ncsu.edu (C. Kleinstreuer).

Nomenclature

Br	Brinkman number
C_p	heat capacity
d_p	nanoparticle diameter
f_D	Darcy friction factor
\vec{g}	body force
h_{nf}	heat transfer coefficient for nanofluids
K_{p-p}	particle–particle interaction intensity
k_{mm}	micro-mixing part for the thermal conductivity k_{nf} of nanofluids
k_{nf}	thermal conductivity of nanofluids
k_{static}	static part for the thermal conductivity k_{nf} of nanofluids
m_p	particle mass
Nu_{nf}	Nusselt number for nanofluids
Po	Poiseuille number
q_w	wall heat flux
R	outer radius of the parallel-disk cooling system
Re	Reynolds number
(r, φ, z)	cylindrical coordinates
\dot{S}_{gen}	entropy generation rate
T	temperature
T_w	wall temperature
T_b	bulk temperature
T_{crit}	critical temperature ($T_{crit} = 310$ K)
U	averaged inlet velocity
(x, y, z)	rectangular coordinates

<i>Greeks</i>	
Φ	shear stress induced heat dissipation
δ	spacing between parallel disks
ζ	damping coefficient
K_B	Boltzmann constant
μ_{nf}	dynamic viscosity of nanofluids
ρ_{nf}	density of nanofluids
τ_p	characteristic time interval
τ_w	wall shear stress
φ	nanoparticle's volume fraction
ω_n	natural frequency

Subscripts and superscripts

bf	base fluid
crit	critical
F	frictional
gen	total entropy generation
H	heat
in	inlet
m	mean
mm	micro-mixing
nf	nanofluid
p	particle
static	static

method into question. For example, Ju et al. [19] analyzed and commented on the error possibilities of the THW method and investigated 20, 30 and 45 nm Al_2O_3 nanoparticle-water suspensions up to a volume fraction of 10%. They did not discover any strong relationship between effective thermal conductivity enhancement and temperature increase. There are other parameters which may influence k_{nf} , e.g., pH value [20] and particle shape/clustering [9,21].

Basic theoretical models for the thermal conductivity of dilute spherical particle suspensions relied on the static model of Maxwell [22]. Hamilton and Crosser [23] extended Maxwell's result to non-spherical particles. For other classical models please refer to Refs. [24–26]. The classical models, based on continuum-mechanics formulations, typically involve only the particle size/shape and volume fraction and assume diffusive heat transfer in both fluid and solid phases. While they provide good predictions for micrometer or larger-size particle suspensions, they usually underestimate any enhanced thermal conductivity increase with volume fraction, nanoparticle diameter, and mixture temperature.

In contrast to the classical models which treat particles stationary to the base fluids, dynamical models take the effect of nanoparticles' random motion into account. The basic mechanisms of anomalous thermal conductivity enhancement of nanofluids are as follows:

- Brownian motion of nanoparticles.
- Liquid molecule-layering on the nanoparticle surface.
- Enhanced heat conduction in the nanoparticles.
- Effect of nanoparticle clustering.

Other mechanisms may be categorized into conduction, nano-scale convection, near-field radiation [27], and thermal wave propagation [28]. The main underlying mechanism of the present F–K model is based on the micro-mixing effect due to Brownian motion. Although Wang et al. [2] and Koblinski et al. [29] concluded that Brownian motion is not a significant mechanism accounting for the anomalous enhancement of the thermal conductivity of

nanofluids, they failed to consider the surrounding fluid motion induced by the random movements of the nanoparticles. Based on in-house research [30], Brownian motion effect is a significant mechanism for the enhancement of the thermal conductivity of nanofluid.

Several theoretical k_{nf} -models have been published based on the Brownian motion effect. For example, Jang and Choi [31] focusing on the heat transfer between nanoparticles and carrier fluid, proposed four modes of energy transport and introduced the idea that a Brownian nanoparticle produces a convection-like effect at the nano-scale. Kumar et al. [32] suggested two models: a stationary particle model and a moving particle model, building a relationship between the effective thermal conductivity and the average particle velocity which is determined by the temperature T . Koo and Kleinstreuer [33] considered the effective thermal conductivity to be composed of two parts: k_{static} is the static thermal conductivity due to the higher thermal conductivity of nanoparticles, following Maxwell's theory, while $k_{Brownian}$ is the enhanced thermal conductivity part generated by the additional convective heat transfer of nanoparticles' Brownian motion and related ambient fluid induced motion. Li [34] extended the model of Koo and Kleinstreuer [33]. Bao [35] also considered the effective thermal conductivity, consisting of a static part and Brownian motion part. Different from the KKL model [34], he only focused on one time interval of Brownian motion, which implies that the velocity of the particle is constant, and treated the ambient fluid around nanoparticle as steady flow. Most recently, a new thermal conductivity theory for nanofluids has been developed, labeled the F–K model; being based on first principles, it does not require any matching functions and predicts benchmark experimental data sets very well [30,36].

One effective cooling device applicable to needs in high-tech industries is the impinging-jet parallel-disk system using nanofluids. However, only a few publications have focused on nanofluid convective heat transfer between two parallel disks [5,6]. Original work on radial flow between rotating (or stationary) disks goes back to McGinn [39], with a most recent contribution by Achintya

[40]. Roy and his research group [5,6] found that for Al₂O₃-water and Al₂O₃-ethylene glycol nanofluids the Nusselt number rapidly increases with elevated alumina volume fractions, say, above 2%. For their numerical calculations they relied on the Maxwell correlation for k_{nf} (see Eq. (7)) which may not be suitable for this case [30,36,37].

Extending a basic mixture-flow analysis which demonstrated the usefulness of the new k_{nf} -model [41], for this paper thermal nanofluid flow between parallel disks has been simulated to present temperature fields and discuss Nusselt numbers as compared to pure water for a realistic heat load. In addition, operational system data as well as entropy generation were analyzed for system-optimization considerations. Based on the extensive literature review, the present computer simulation of radial thermal nanofluid flow between parallel disks and entropy-minimization analysis best device design are novel contributions.

2. Theory

The dilute suspensions of nanoparticles in water of the radial cooling system (see Fig. 1) were assumed to be Newtonian mixtures in steady 3D laminar non-isothermal flow.

2.1. Modeling equations

Assuming steady laminar incompressible 3D flow, the conservation laws can be written as:

$$\nabla \cdot (\rho_{nf} \vec{v}) = 0 \tag{1}$$

$$\nabla(\rho_{nf} \vec{v} \vec{v}) = \nabla p + \nabla \cdot (\mu_{nf} \nabla \vec{v}) + \vec{g} \tag{2}$$

$$\vec{v} \cdot \nabla T = \frac{\nabla \cdot (k_{nf} \nabla T)}{(\rho c_p)_{nf}} + \frac{\Phi}{(\rho c_p)_{nf}} \tag{3}$$

where subscript nf denotes “nanofluid” and Φ is the shear stress induced energy dissipation in cylindrical coordinates, i.e.,

$$\Phi = \mu_{nf} \left\{ \left(\frac{\partial v_\theta}{\partial z} + \frac{1}{r} \frac{\partial v_z}{\partial \theta} \right)^2 + \left(\frac{\partial v_z}{\partial r} + \frac{\partial v_r}{\partial z} \right)^2 + \left(\frac{1}{r} \frac{\partial v_r}{\partial \theta} + r \frac{\partial}{\partial r} \left(\frac{\partial v_\theta}{\partial r} \right) \right)^2 + 2 \left(\left(\frac{\partial v_r}{\partial r} \right)^2 + \left(\frac{1}{r} \left(\frac{\partial v_\theta}{\partial \theta} + v_r \right) \right)^2 + \left(\frac{\partial v_z}{\partial z} \right)^2 \right) \right\} \tag{4}$$

Concerning the necessary boundary conditions, we assumed uniform inlet velocity and pressure outlet, constant wall heat flux q_w , no-slip condition at the heated upper disk ($r \in [0, R]$, $z = 0$) as well as adiabatic and no-slip conditions at all other walls (see Fig. 1).

2.2. Nanofluid properties

The nanofluid properties are mainly a function of nanoparticle volume fraction φ and mixture temperature T . Specifically, for dilute Al₂O₃-water nanofluids [34]:

$$\mu_{nf} = \mu_{bf} \frac{1}{(1 - \varphi)^{2.5}} \tag{5a}$$

$$\rho_{nf} = \varphi \rho_p + (1 - \varphi) \rho_{bf} \tag{5b}$$

$$(\rho c_p)_{nf} = \varphi (\rho c_p)_p + (1 - \varphi) (\rho c_p)_{bf} \tag{5c}$$

For the effective thermal conductivity of the nanofluid, the newly developed Feng–Kleinstreuer (F–K) model [3,4] was applied. In summary, it was postulated that the thermal conductivity of nanofluids consists of a static part (k_{static}) after Maxwell [22] and a micro-mixing part (k_{mm}), i.e., enhancement due to Brownian motion of nanoparticles. Thus, k_{nf} of the F–K model is expressed as:

$$k_{nf} = k_{static} + k_{mm} \tag{6}$$

The static part is given by Maxwell’s model as:

$$k_{static} = \left(1 + \frac{3 \left(\frac{k_p}{k_{bf}} - 1 \right) \varphi}{\left(\frac{k_p}{k_{bf}} + 2 \right) - \left(\frac{k_p}{k_{bf}} - 1 \right) \varphi} \right) k_{bf} \tag{7}$$

while the micro-mixing part is given by:

$$k_{mm} = 49500 \cdot \frac{K_B \tau_p}{2m_p} \cdot c_c \cdot (\rho c_p)_{nf} \cdot \varphi^2 \cdot (T \ln T - T) \cdot \frac{\exp(-\zeta \omega_n \tau_p) \sinh \left(\sqrt{\frac{(3\pi\mu_{bf}d_p)^2}{4m_p^2} - \frac{K_{p-p}}{m_p} \frac{m_p}{3\pi\mu_{bf}d_p}} \right)}{\tau_p \sqrt{\frac{(3\pi\mu_{bf}d_p)^2}{4m_p^2} - \frac{K_{p-p}}{m_p}}} \tag{8}$$

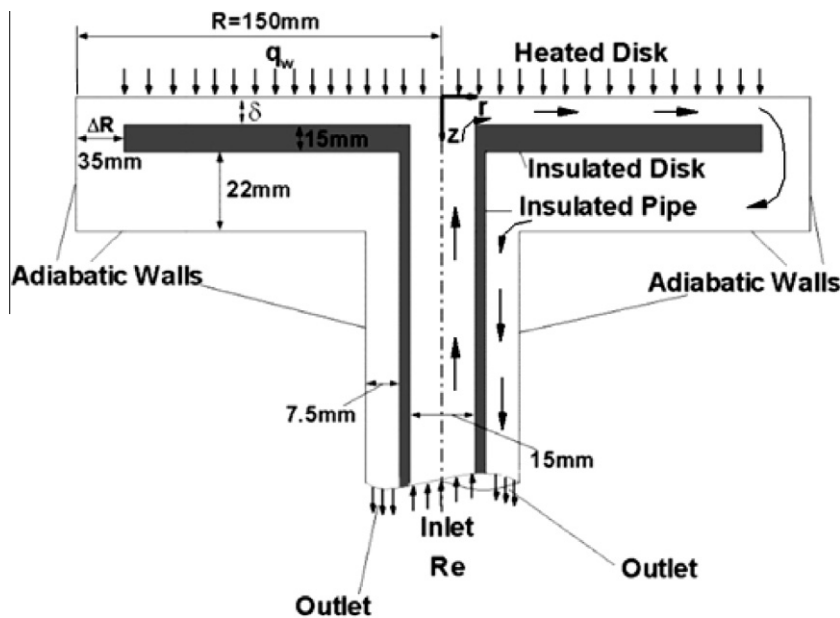


Fig. 1. Sketch of the radial flow cooling system.

Here, ρ is the density, c_p is the specific heat capacity, ϕ is the nanoparticle volume fraction, while the subscripts nf, bf, and p indicate nanofluid mixture, base fluid and particle, respectively. c_c is equal to 38 for metal-oxide nanofluids which can be derived theoretically instead of being obtained via a curve-fitting technique. The damping coefficient ζ , natural frequency ω_n , and characteristic time interval τ_p can be expressed as:

$$\zeta = \frac{3\pi d_p \mu_{bf}}{2m_p \omega_n} \quad (9)$$

$$\omega_n = \sqrt{\frac{K_{p-p}}{m_p}} \quad (10)$$

$$\tau_p = \frac{m_p}{3\pi \mu_{bf} d_p} \quad (11)$$

Specifically, for metal-oxide nanofluids, the magnitude of particle-particle interaction intensity K_{p-p} is determined as:

$$K_{p-p} = \rho_p \cdot \sqrt{d_p} \cdot \left(\frac{32.1724 \cdot 273K}{T} - 19.4849 \right) \quad (12)$$

In light of experimental evidence, the F-K model is suitable for several types of metal-oxide nanoparticles ($30 < d_p < 50$ nm) in water with volume fractions up to 5%, and mixture temperatures below 350 K. The properties of the base fluid, i.e., water, vary with temperature as follows [34]:

$$\rho_{\text{water}} = 1000 \cdot \left(1 - \frac{(T + 15.7914)}{508929.2 \cdot (T - 205.0204)} \right) \cdot (T - 277.1363)^2 \quad (13a)$$

$$c_{p,\text{water}} = 9616.8734 - 48.7365 \cdot T + 0.1445 \cdot T^2 - 0.0001414 \cdot T^3 \quad (13b)$$

$$\mu_{\text{water}} = 0.02165 - 0.0001208 \cdot T + 1.7184e - 7 \cdot T^2 \quad (13c)$$

$$k_{\text{water}} = -1.1245 + 0.009734 \cdot T - 0.00001315 \cdot T^2 \quad (13d)$$

Different types of nanofluids were employed in the application of nanofluid flow of an impinging-jet between parallel disks, requiring a numerical solution method. However, assuming quasi-fully-developed flow beyond the inlet region (see Fig. 1) allowed for analytical solutions of velocity profiles, pressure drop and friction factor in the r -direction, as given by Feng and Kleinstreuer [41].

3. Numerical method

The numerical solutions were executed with a user-enhanced finite volume method, i.e., ANSYS-CFX 11.0 and 12.0 from Ansys, Inc. (Canonsburg, PA). The computations were performed on an IBM Linux Cluster at North Carolina State University's High Performance Computing Center (Raleigh, NC) and on a local dual Xeon Intel 3.0G Dell desktop (Computational Multi-Physics Laboratory, MAE Department, NC State University). For example, the unstructured mesh for the $\delta = 3$ mm model contained 646, 258 hexahedral elements. In light of the large velocity and temperature gradients, which exist at the corners and near the boundaries, the local mesh was refined locally by a factor of 1.05. For the $\delta = 1, 2$ and 4 mm models, the same unstructured mesh-generation method was employed. The criterion of convergence was $1e-5$ for the maximum residual which guaranteed an average residual of less than $1e-6$ for both momentum and heat transfer. Mesh independence was examined and verified by increasing the element number by 100% in each direction which produced a maximum result change of just 2.53%. A typical numerical simulation case took 28–38 h. The computer-model was further validated by comparing numerical solutions of velocity and temperature fields with our analytical solution [9] as well as existing numerical and experimental data sets [30]. Additional comparisons with experimental observations are given in Section 4.1.

4. Results and discussion

4.1. Model comparisons

Of interest is how the measurements performed by Gherasim et al. [38] compare to the numerical results using the new F-K model. Fig. 2 shows the radial (upper) wall temperatures for the 4% Al_2O_3 -water nanofluid with the heat flux $q_w = 2438 \text{ W/m}^2$ and mass flow rate $\dot{m} = 0.019 \text{ kg/s}$. Although the trends of the distributions are somewhat similar, there is a large difference in the region $0 < r < 100$ mm when compared to the data of Gherasim et al. [6]. It is worth mentioning that the lower, nonlinear temperature distribution with a local peak-value in the inlet zone is more realistic; because, local vortical flow which leads to nanofluid circulation generated overall a slightly stronger cooling effect of the upper disk

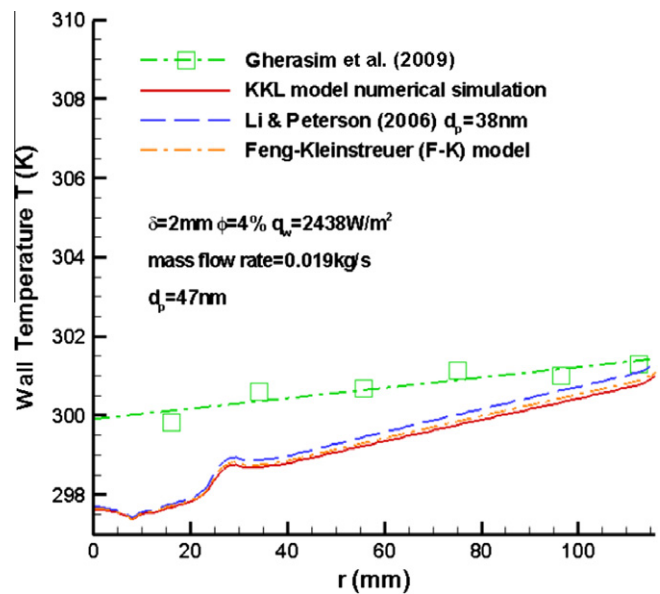


Fig. 2. Numerical simulation results for radial wall temperature distribution using the Feng-Kleinstreuer model as compared to experimental measurements.

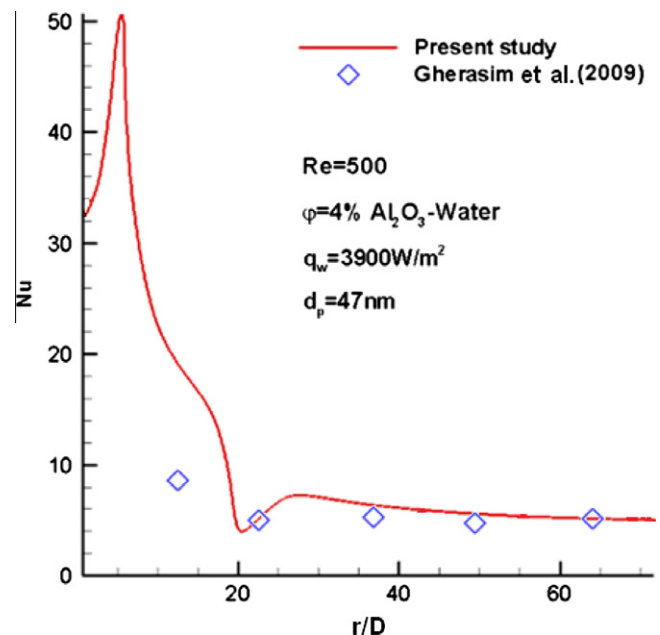


Fig. 3. Nusselt number comparison between present numerical simulation and experimental data.

wall (~2 K) than the experimental data indicates. In contrast, outside the lower-disk inlet zone the radial Nusselt number results compare well with the measurements of Gherasim et al. [6], as shown in Fig. 3. As the $T_{bulk}(r)$ -calculation is correct, it can be assumed that the experimentally based evaluation of the bulk temperature is flawed; however, when forming the ratio for the Nusselt number distribution (see Fig. 3) the induced temperature-errors canceled. Additional successful computer-model validations with different experimental data sets are given by Feng [30].

4.2. Fluid flow structures

Important for convection heat transfer in this impingement-jet, parallel-disk system are the velocity fields near the inlet as well as the nanofluid flow developments for different inlet Reynolds numbers. Fig. 4(a–c) indicates that near the conjunction of inlet pipe and parallel disks, the flow separation area becomes larger with the increase in Reynolds number, Re. At Re = 150, the separation area (1st recirculation cell) is hardly noticeable and there is no

2nd recirculation cell downstream. At Re = 300, the separation area becomes larger and the 2nd recirculation cell can be observed, but it is still very small. At Re = 500, two recirculation cells are apparent. While the flow field in the T-junction entrance region remains very similar for all (laminar) Reynolds numbers, i.e., $150 < Re < 500$, the slit-flow structure in the parallel-disk exit region varies more when $Re > 300$. We can conclude that the velocity field is smoother at lower Reynolds numbers which, in turn, may generate a smoother temperature field for, say, $200 < Re < 400$.

4.3. Entrance length vs. inlet Reynolds number

According to the analytical solution for quasi-fully-developed flow between parallel disks, the velocity profile in the r -direction can be expressed as [30]:

$$v_r = \frac{6R_{in}V_{in}^s}{\delta^2} \frac{1}{r}(\delta - z)z = \frac{3 \cdot R_{in}^2 \cdot V_{in}}{\delta^3} \frac{1}{r}(\delta - z)z \tag{14}$$

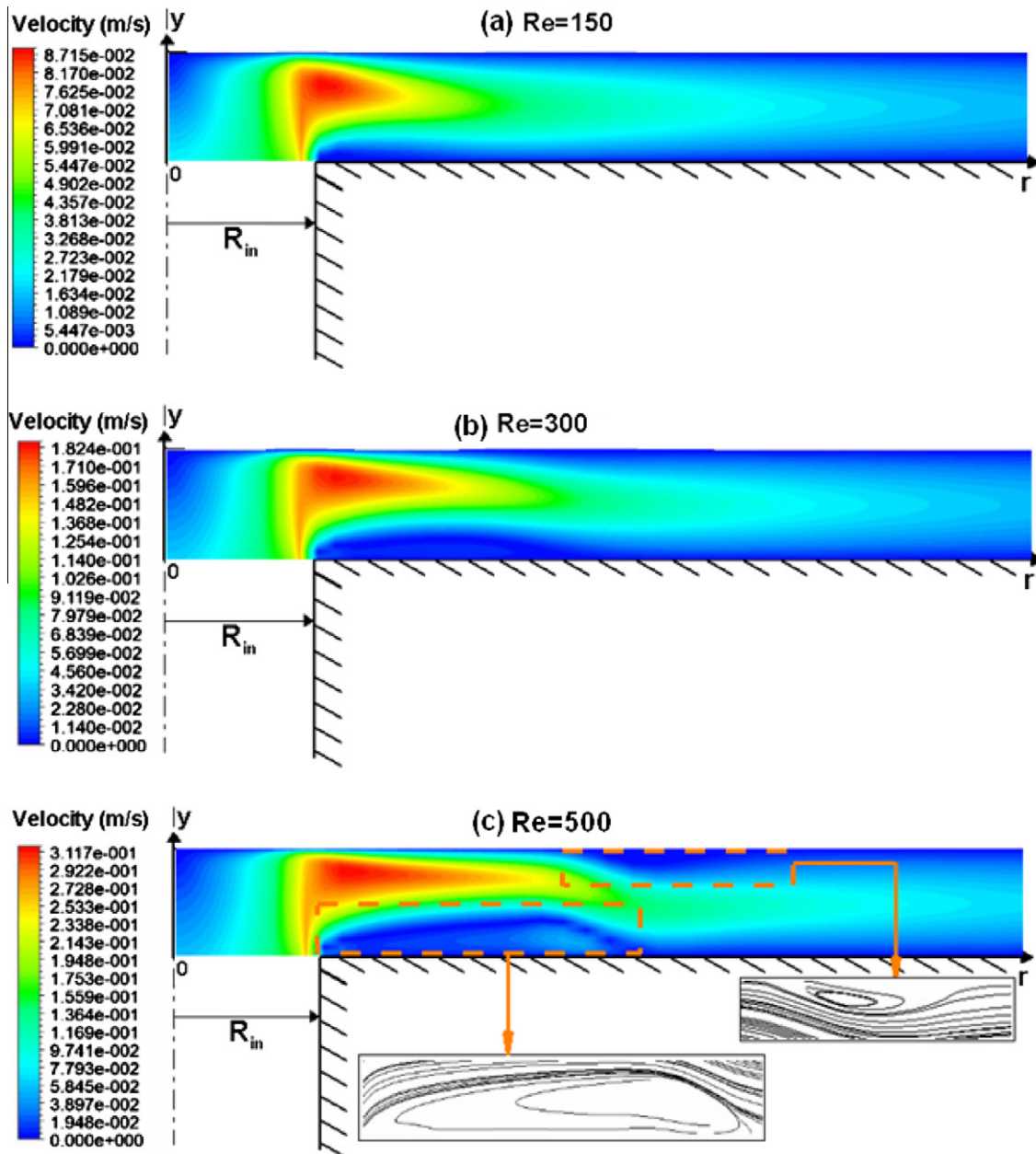


Fig. 4. (a–c) Velocity contours for cooling system subject to different inlet Reynolds numbers (4% Al₂O₃-water $T_{in} = 297$ K, $q_w = 10,000$ W/m², $d_p = 47$ nm, $\delta = 2$ mm).

As expected, the maximum velocity exists at $z = \delta/2$. Without losing generality, $\delta = 2$ mm was chosen to determine the relationship between normalized entrance length R_{crit}/R and inlet Reynolds number, i.e., $150 < Re_{in} < 1000$. The criterion to identify the end of the radial inlet region is the maximum velocity difference between numerical solution and analytical solution being less than 5%. According to Fig. 5, R_{crit}/R linearly increases with the increment of Re_{in} . A linear relationship can be given for $\delta = 2$ mm as:

$$\frac{R_{crit}}{R} = 0.0004708Re_{in} + 0.09554 \quad Re_{in} \in [150, 1000] \quad (15)$$

for which the curve-fitting r -square is 0.9975.

4.4. Poiseuille number: nanofluid vs. pure water

The Poiseuille number (Po) is defined here as:

$$Po = f_D \cdot Re_{nf}^{in} \quad (16)$$

where

$$f_D = \frac{4\tau_w}{\frac{1}{2}\rho_{nf}\bar{v}^2} \quad (17a)$$

and

$$Re_{nf}^{in} = \frac{\rho_{nf}V_{in}(2\delta)}{\mu_{nf}} \quad (17b)$$

The radial Poiseuille number (Po#) for pure water and the 4% Al_2O_3 -water nanofluid ($d_p = 38.4$ nm) with inlet Reynolds number $Re = 400$ and heat flux $q_w = 10$ kW/m² were investigated for two inlet temperatures. The comparison results are shown in Fig. 6. The complex flow field in the inlet region (see Fig. 3) results in strong variations of the local wall shear stress and hence in Po# for $0 < r < 0.04$ m (see Eq. (15a)). As expected, $Po_{nanofluid} > Po_{water}$ for the same inlet temperature; however, when T_{in} is increased the Po# decreases because of the reduced fluid viscosity and hence lower friction factor. In summary, the small increases in wall shear stress when using nanofluids will not cause a noticeable penalty on pumping power. Additionally, when viewing Figs. 4(a–c) and 6, it is necessary to mention that the inlet region

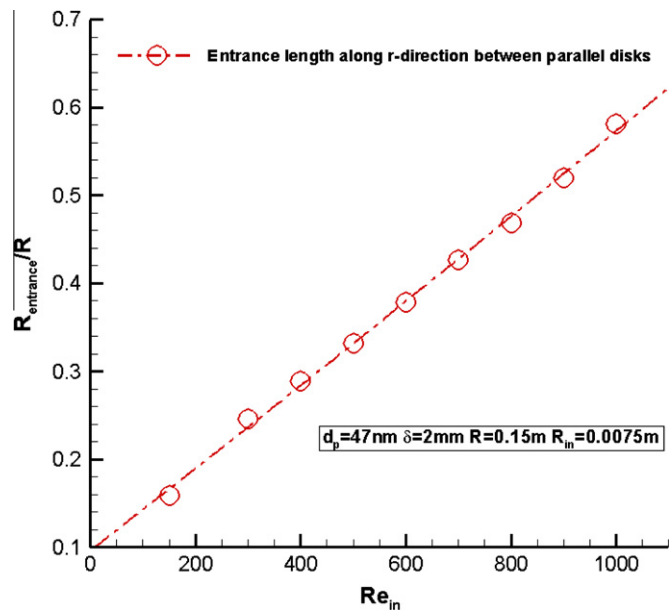


Fig. 5. Normalized entrance length vs. inlet Reynolds number (4% Al_2O_3 -water $T_{in} = 297$ K, $q_w = 10,000$ W/m², $d_p = 47$ nm, $\delta = 2$ mm).

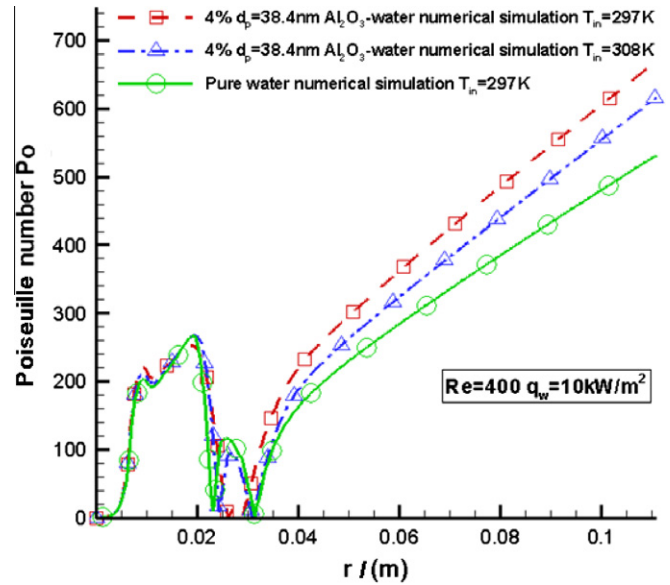


Fig. 6. Radial Poiseuille numbers for water and nanofluids with different inlet temperatures.

approximately ends at $r = 0.05$ m after which the flow can be considered to be quasi-fully-developed with smooth velocity and temperature fields.

4.5. Temperature fields

4.5.1. Inlet Reynolds number effect

Fig. 7(a–c) shows nanofluid temperature contours for different inlet Reynolds numbers. As can be deduced from Fig. 8(a), given the thermal load of 10 kW/m², the Reynolds number has to be sufficiently high to achieve wall temperatures below a critical value for proper device functioning, e.g., $Re_{in} > 400$ to maintain $T_w < 40$ °C (312 K). However, as the Reynolds number increases to 500, because of the second recirculation zone appearing near the upper disk (see Fig. 4), complex local flow fields may cause more non-uniform wall temperatures.

4.5.2. Nanoparticle volume-fraction effect

For comparison, pure water, 4% Al_2O_3 -water nanofluid ($d_p = 38.4$ nm) and 4% Al_2O_3 -water nanofluid ($d_p = 30$ nm) were investigated. The nanofluids produce lower wall temperatures at the upper disk (see Fig. 8(a)) than the pure water case; and, as the volume fraction ϕ increases the wall temperature decreases further. Clearly, the elevated thermal conductivities of the mixtures (see Eq. (6)) cause better heat transfer than just water. Interestingly, when compared to pure liquids, nanofluids “dampen” the complex flow fields and thereby generating smoother temperature fields. Specifically, with the increase in ϕ , the local wall temperature and local bulk temperature of nanofluids decrease which lead to an increase in viscosity μ_{nf} (see Eqs. (5a) and (13c)). Thus, an increase in viscosity makes the fluid more stable, e.g., delaying/smoothing eddy generation. It can be concluded that both wall temperature and bulk temperature decrease with the increase in nanoparticle volume fraction. Also, k_{nf} increases with decreasing nanoparticle diameter and that impact on the wall temperature is depicted in Fig. 8(a). However, the temperature differences caused by different nanoparticle sizes are not very large (i.e., less than 1 K).

4.5.3. Maximum wall temperature control

Of interest are operational and geometric device data which assure that the maximum wall temperature stays below a critical

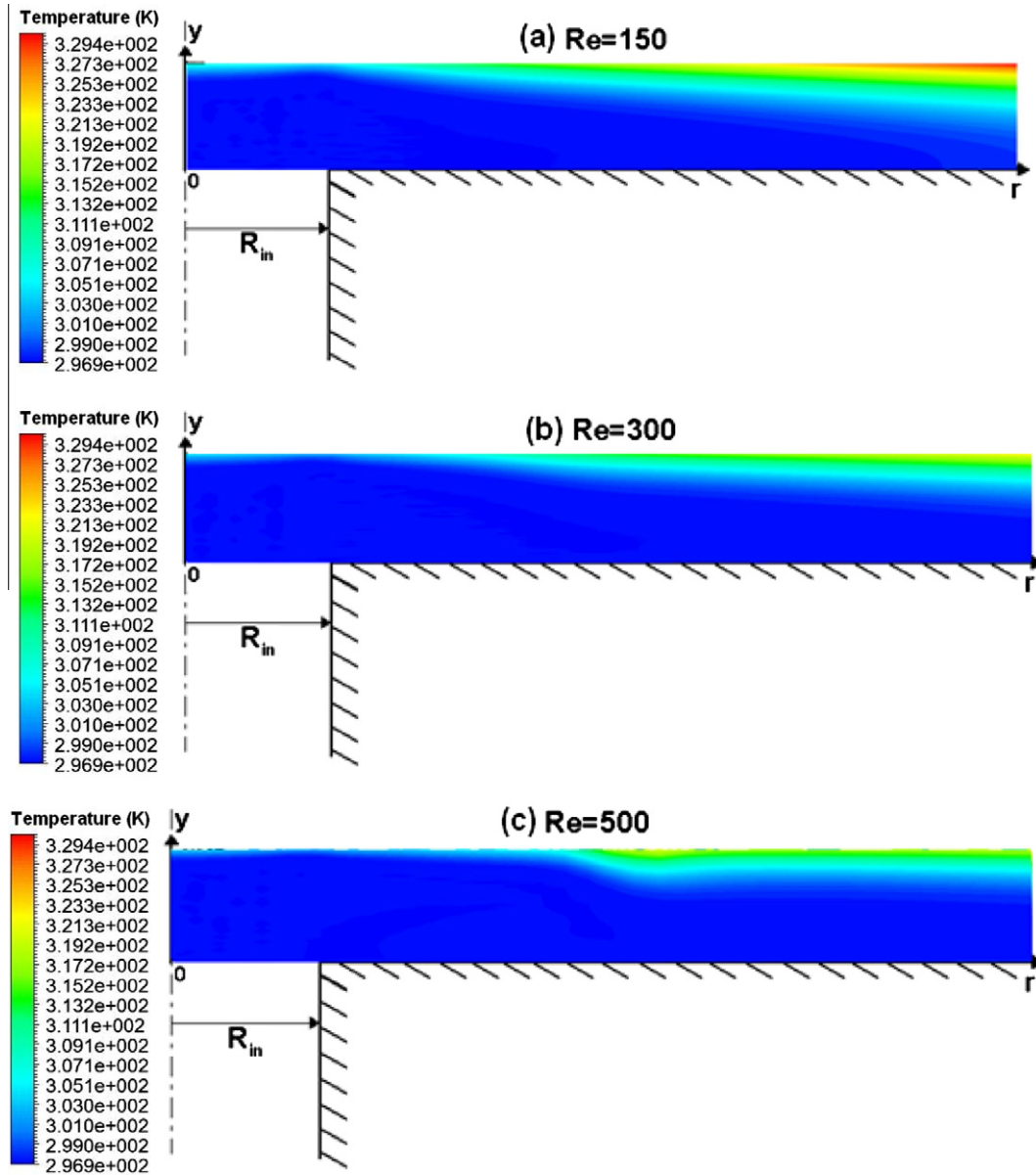


Fig. 7. (a–c) Temperature contours for cooling system with different inlet Reynolds numbers (4% Al₂O₃-water $T_{in} = 297$ K, $q_w = 10,000$ W/m², $d_p = 47$ nm, $\delta = 2$ mm).

temperature, T_{crit} . Using nanofluids instead of pure water allows wall temperature control with relatively low inlet Reynolds numbers, which is desirable to avoid the more complicated radial slit-flow structures. For the system with $\delta = 1$ mm (see Fig. 1), we assumed T_{crit} be 40 °C (312 K). To utilize the better nanofluid convective heat transfer, the maximum wall temperature was controlled to remain under 310 K by using a 5% ($d_p = 30$ nm) Al₂O₃-water nanofluid as the coolant with a relatively low Reynolds number of 300 for $q_w = 10$ kW/m². Also, for $q_w = 20$ kW/m², Re needs to be increased to 1200 to achieve the temperature controlling goal. The new radial wall temperature distributions are shown in Fig. 8(b).

4.6. Nanofluid Nusselt number

The Nusselt number of a nanofluid is defined as:

$$Nu_{nf} = \frac{h_{nf} D_h}{k_{water}} \quad (18)$$

with

$$h_{nf} = \frac{q_w}{T_w - T_b} \quad (19)$$

where q_w is the wall heat flux, T_w is the wall temperature, and T_b is the bulk temperature of the mixture, while D_h is the characteristic length, e.g., $D_h = 2\delta$. Instead of using the variable k_{nf} , k_{water} was employed in the definition of the Nusselt number; implying, that when using k_{nf} an increase of k_{nf} would mathematically disguise the actual increase in Nusselt number when using nanofluids as coolants. Furthermore, the mean Nusselt number Nu_{nf}^m and mean heat transfer coefficient h_{nf}^m can be defined as follows:

$$Nu_{nf,m} = \frac{1}{R^2} \int_0^R 2Nu_{nf} r dr \quad (20)$$

$$h_{nf,m} = \frac{1}{R^2} \int_0^R 2h_{nf} r dr \quad (21)$$

Here, h_{nf} and Nu_{nf} indicate the convective heat transfer ability of the nanofluid, i.e., the higher an h_{nf} value is the better is the convection heat transfer.

For tubular nanofluid flow Li [42] proposed in general:

$$Nu_{nf} = f\left(Re_{nf}, Pr_{nf}, \frac{k_p}{k_{bf}}, \frac{(\rho c_p)_p}{(\rho c_p)_{nf}}, \phi, Pe, \text{etc.}\right) \quad (22)$$

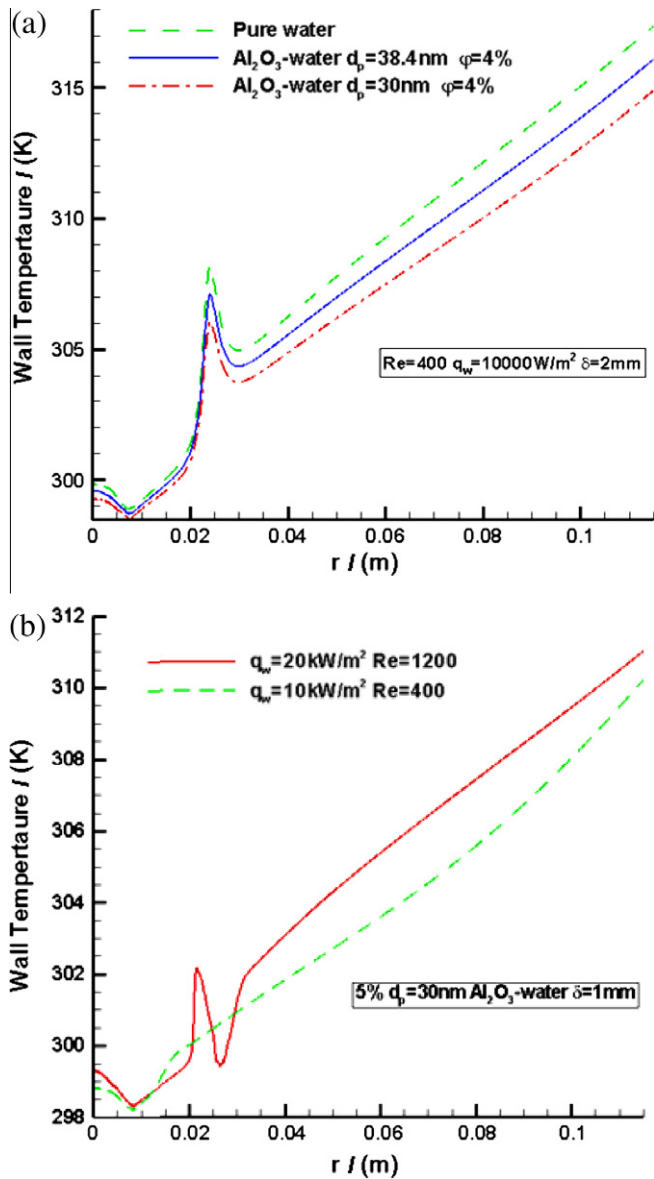


Fig. 8. (a) Wall temperature distributions for Al₂O₃-water nanofluids and pure water. (b) Controlled wall temperature distributions using Al₂O₃-water nanofluid ($\phi = 5\%$, $Re = 600$ and $\delta = 1$ mm, assuming $q_w = 10$ kW/m²; $\phi = 5\%$, $Re = 1200$ and $\delta = 1$ mm, assuming $q_w = 20$ kW/m²).

where $Re_{nf} = (\bar{v} \cdot 2\delta)/\nu_{nf}$ is the nanofluid Reynolds number, $Pr_{nf} = \nu_{nf}/\alpha_{nf}$ is the Prandtl number, $Pe = (\bar{v} \cdot d_p)/\alpha_{nf}$ is the Peclet number, and $\alpha_{nf} = k_{nf}/(\rho c_p)_{nf}$. In contrast, considering the characteristics of impinging-jet flow between parallel disks for the given Al₂O₃-water nanofluid, we postulate:

$$Nu_{nf,m} = f(Re_{nf}, Br_{nf,m}) \quad (23)$$

where Br_{nf} is the nanofluid Brinkman number which is defined as:

$$Br_{nf} = \frac{\mu_{nf} U^2}{q_w \delta} \quad (24)$$

Here, U is the characteristic velocity which is the average inlet velocity, and δ is the spacing between the disks which was varied. It can be assumed that the Nusselt number and heat transfer coefficient are not strongly dependent on the Prandtl number; actually, Pr_{nf} changes only from 4 to 5. The wall heat flux was doubled to elucidate stronger thermal effects.

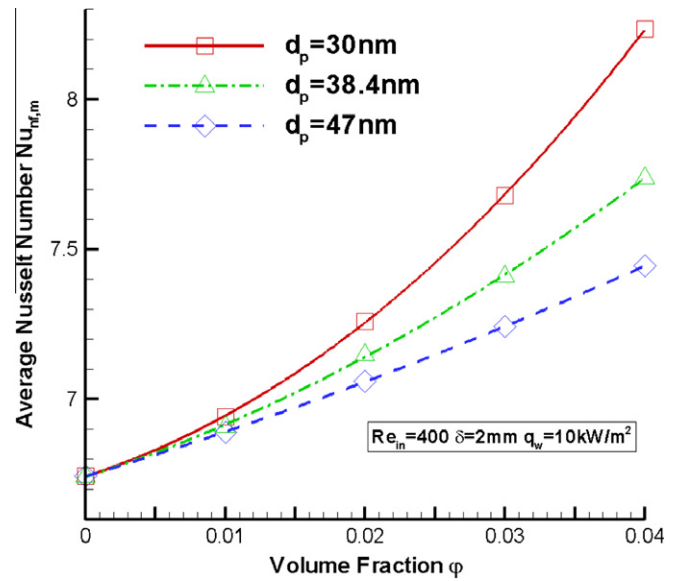


Fig. 9. Nusselt number vs. nanoparticle volume fraction and nanoparticle diameter.

Fig. 9 shows the relationship between the average $Nu_{nf,m}$ for the upper disk and the nanoparticle volume fraction and diameter. Clearly, higher volume fractions indicate better convective heat transfer performance and thereby providing higher $Nu_{nf,m}$ values. Also, with a decrease in particle diameter, the Brownian motion of nanoparticles is enhanced and hence $Nu_{nf,m}$ increases. To the authors' knowledge, the dependence of Nusselt number on nanoparticle volume fraction and nanoparticle diameter has not been discussed before.

Fig. 10 shows the relationship between the average $Nu_{nf,m}$ for the upper disk and the average Brinkman number $Br_{nf,m}$ of the system with certain values for the Reynolds number, i.e., $Re = 200, 400, 600$ and 800 , while the disk-spacing was varied from 1 to 4 mm. Nu_{nf} increases dramatically with the $Br_{nf}\#$ for each Re_{in} value, which implies that with the decrease in spacing δ the system provides a better convective heat transfer performance. It is worth

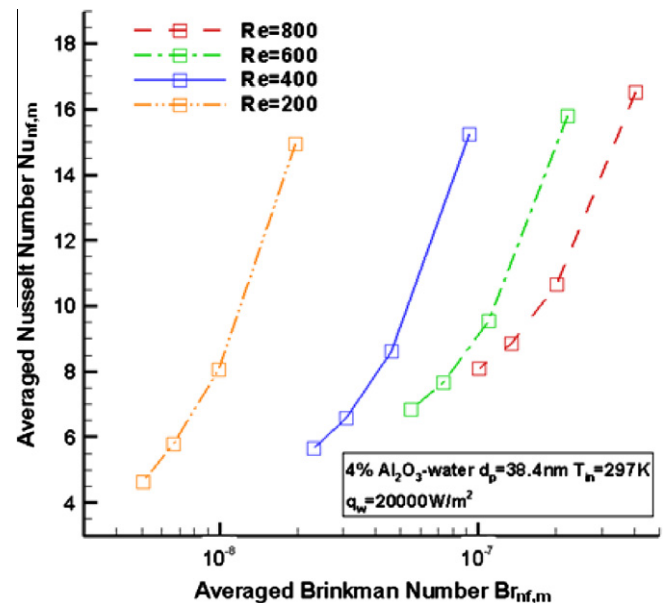


Fig. 10. Relationship between Nusselt number and Brinkman number with different disk-spacing for different Reynolds numbers and at $q_w = 20$ kW/m².

emphasizing that the Brinkman number is usually only used in studies of flow through porous media. Here, the Brinkman number for nanofluid flow (see Eq. (24)) combines an essential mixture property with nanofluid flow, heat transfer and geometric parameters. Such a dimensionless group is essential for the study of the heat transfer performance of nanofluids.

4.7. Entropy generation analysis

Entropy generation analysis is a modern method to evaluate the efficiency of a system and thus optimize a device performance by evaluating best geometric and operational parameter values as well as suitable fluid-properties. The entropy generation rate per unit volume can be expressed as [34]:

$$\dot{S}_{gen}''' = \frac{k}{T^2} (\nabla T)^2 + \frac{\Phi}{T} = \dot{S}_{gen}'''^{(H)} + \dot{S}_{gen}'''^{(F)} \quad (25)$$

where for the present case the entropy source due to heat transfer is much larger than the one caused by frictional effects, i.e., $\dot{S}_{gen}'''^{(H)} \gg \dot{S}_{gen}'''^{(F)}$.

For starters, the relationship between entropy generation rate and inlet Reynolds number as well as inlet temperature are investigated. Fig. 11 shows that with the increasing inlet temperature the total entropy generation rate decreases because both the thermal and frictional contributions decrease; however, at quite different magnitudes. For geometry optimization, the relationship between entropy generation rate and the spacing between parallel disks δ was investigated and the results are shown in Fig. 12. The total frictional entropy generation rate decreases with an increase in δ , while the total thermal transfer entropy generation rate increases with the increase in δ . Recalling that $S^H \gg S^F$, the total entropy generation rate increases with an increase in δ . Hence, it can be concluded that a smaller disk-spacing is able to provide higher cooling efficiency for the system.

Considering pure water, $\varphi = 0$, and 4% Al₂O₃-water nanofluid ($d_p = 38.4$ nm), the influence of nanoparticle volume fraction φ on the entropy generation rate in the cooling system was analyzed. Fig. 13 provides the total entropy generation rate for the whole flow region (see Fig. 1), which decreases with increasing volume

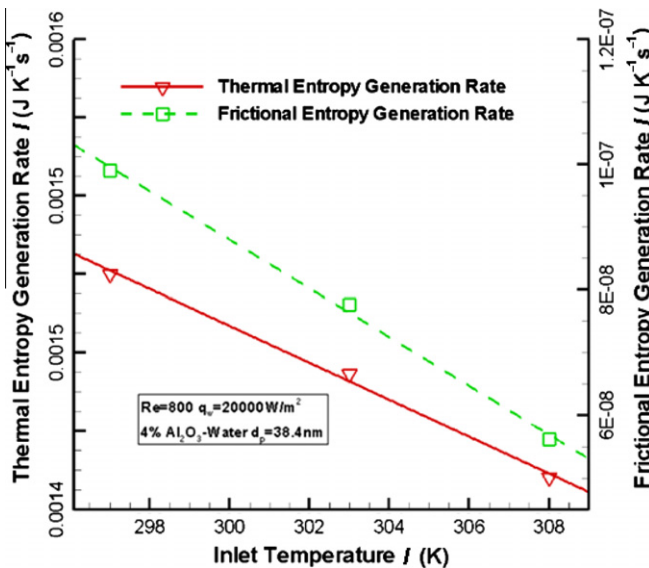


Fig. 11. Thermal and frictional entropy generation rates for 4% $d_p = 38.4$ nm Al₂O₃-water nanofluids at Re = 800 and for $q_w = 20$ kW/m².

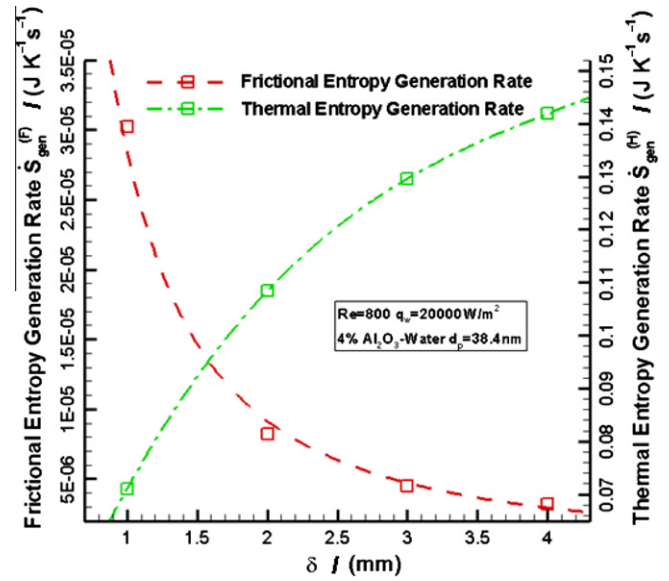


Fig. 12. Thermal and frictional entropy generation rates as a function of disk-spacing δ for 4% $d_p = 38.4$ nm Al₂O₃-water nanofluid with Re = 800 and $q_w = 20$ kW/m².

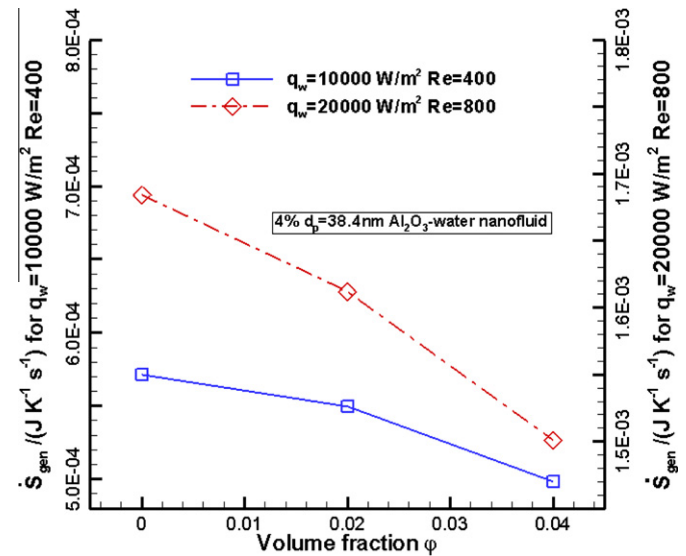


Fig. 13. Total entropy generation rate for $d_p = 38.4$ nm Al₂O₃-water nanofluid (Re = 400 and $q_w = 10$ kW/m²; Re = 800 and $q_w = 20$ kW/m²).

fraction. Hence, using nanofluids may lead to improved system-performance efficiencies when compared to pure water.

5. Conclusions

Using a new, experimentally validated model for the thermal conductivity of nanofluids, numerical simulations have been executed for alumina-water nanofluid flow with heat transfer between parallel disks. The results indicate that nanofluids are promising new coolants when compared to pure water. Specifically, smoother mixture flow fields and temperature distributions can be achieved. Given realistic thermal loads (here $q_w = 10$ and 20 kW/m²), the Nusselt number increases with higher nanoparticle volume fraction, smaller nanoparticle diameter, reduced

disk-spacing, and, of course, larger inlet Reynolds number. Furthermore, nanofluids reduce the system's total entropy generation rate while hardly increasing the required pumping power for any given Re_{in} . Fully-developed flow can be assumed after a critical radial distance, expressed in a correlation $Re_{crit} = fct(Re_{in})$, has been reached and hence analytic solutions provide good approximations. Minimization of total entropy generation allows for operational and geometric system-optimization in terms of $S_{gen} = fct(Re \text{ and } \delta)$.

Acknowledgements

The authors appreciate and acknowledge the use of ANSYS (V. 11 and V. 12) from ANSYS Inc. (Canonsburg, PA), made available by Dr. Helen Redshaw (Department of Domestic Partnerships). Also, the authors appreciate and acknowledge the Chinese Scholarship Council (CSC) for financial support of Yu Feng.

References

- [1] S. Lee, S.U.S. Choi, Measuring thermal conductivity of fluids containing oxide nanoparticles, *J. Heat Transfer* 121 (1999) 280–289.
- [2] X.W. Wang, X.F. Xu, S.U.S. Choi, Thermal conductivity of nanoparticle–fluid mixture, *J. Thermalphys. Heat Transfer* 13 (1999) 474–480.
- [3] J.A. Eastman, S.U.S. Choi, S. Li, W. Yu, L.J. Thompson, Anomalous increased effective thermal conductivities of ethylene glycol-based nanofluids containing copper nanoparticles, *Appl. Phys. Lett.* 78 (6) (2001) 718–720.
- [4] C.H. Li, G.P. Peterson, Experimental investigation of temperature and volume fraction variations on the effective thermal conductivity of nanoparticle suspensions (nanofluids), *J. Appl. Phys.* 99 (8) (2006) 084314.
- [5] H. Xie, J. Wang, T. Xi, Y. Liu, Thermal conductivity of suspensions containing nanosized SiC particles, *Int. J. Thermophys.* 23 (2) (2002) 571–580.
- [6] T.K. Hong, H.S. Yang, C.J. Choi, Study of enhanced thermal conductivity of Fe nanofluids, *J. Appl. Phys.* 97 (6) (2005) 1–4.
- [7] M. Chopkar, S. Sudarshan, P.K. Das, I. Manna, Effect of particle size on thermal conductivity of nanofluid, *Metall. Mater. Trans. A* 39A (2008) 1535–1542.
- [8] H.A. Mintsa, G. Roy, C.T. Nguyen, D. Doucet, New temperature dependent thermal conductivity data for water-based nanofluids, *Int. J. Therm. Sci.* 48 (2009) 363–371.
- [9] S.M.S. Murshed, K.C. Leong, C. Yang, Enhanced thermal conductivity of TiO₂-water based nanofluids, *Int. J. Therm. Sci.* 44 (2005) 367.
- [10] W. Duangthongsuk, S. Wongwaises, Measurement of temperature-dependent thermal conductivity and viscosity of TiO₂-water nanofluids, *Exp. Therm. Fluid Sci.* 33 (2009) 706–714.
- [11] S.K. Das, N. Putra, P. Theisen, W. Roetzel, Temperature dependence of thermal conductivity enhancement for nanofluids, *J. Heat Transfer* 125 (2003) 567–574.
- [12] H.E. Patel, S.K. Das, T. Sundararajan, N.A. Sreekumar, B. George, T. Pradeep, Thermal conductivities of naked and monolayer protected metal nanoparticle based nanofluids: manifestation of anomalous enhancement and chemical effects, *Appl. Phys. Lett.* 83 (2003) 2931–2933.
- [13] E.V. Timofeeva, A.N. Gavrilov, J.M. McCloskey, Y.V. Tolmachev, Thermal conductivity and particle agglomeration in alumina nanofluids: experiment and theory, *Phys. Rev. E* 76 (2007) 061203-1–061203-16.
- [14] R. Rusconi, E. Rodari, R. Piazza, Optical measurement of thermal properties of nanofluids, *Appl. Phys. Lett.* 89 (2006) 261916-1–261916-3.
- [15] S.A. Putnam, D.G. Cahill, P.V. Braun, Thermal conductivity of nanoparticle suspensions, *J. Appl. Phys.* 99 (2006) 084308-1–084308-6.
- [16] D.C. Venerus, M.S. Kabadi, S. Lee, V. Perez-Luna, Study of thermal transport in nanoparticle suspension using forced Raleigh scattering, *J. Appl. Phys.* 100 (2006) 094310-1–094310-8.
- [17] W. Williams, J. Buongiorno, L.W. Hu, Experimental investigation of turbulent convective heat transfer and pressure loss of alumina/water and zirconia/water nanoparticle colloids (nanofluids) in horizontal tubes, *J. Heat Transfer* 130 (2008) 042412-1–042412-7.
- [18] B. Kolade, K. Goodson, J.K. Eaton, Convective performance of nanofluids in a laminar thermally developing tube flow, *J. Heat Transfer* 131 (2009) 052402-1–052402-8.
- [19] Y.S. Ju, J. Kim, M.T. Hung, Experimental study of heat conduction in aqueous suspensions of aluminum oxide nanoparticles, *J. Heat Transfer* 130 (2008) 092403-1–092403-6.
- [20] D. Zhu, X. Li, N. Wang, X. Wang, J. Gao, H. Li, Dispersion behavior and thermal conductivity characteristics of Al₂O₃-H₂O nanofluids, *Curr. Appl. Phys.* 9 (2009) 131–139.
- [21] H.T. Zhu, C.Y. Zhang, Y.M. Tang, J.X. Wang, Novel synthesis and thermal conductivity of CuO nanofluid, *J. Phys. Chem. C* 111 (2007) 1646.
- [22] J.C. Maxwell, *A Treatise on Electricity and Magnetism*, third ed., Clarendon Press, Oxford, UK, 1891.
- [23] R.L. Hamilton, O.K. Crosser, Thermal conductivity of heterogeneous two component systems, *Ind. Eng. Chem. Fundam.* 1 (1962) 187–191.
- [24] D.J. Jeffrey, Conduction through a random suspension of spheres, *Proc. R. Soc. A* 335 (1973) 355–367.
- [25] R.H. Davis, The effective thermal conductivity of a composite material with spherical inclusions, *Int. J. Thermophys.* 7 (1986) 609–620.
- [26] D.A.G. Bruggeman, Berechnung verschiedener physikalischer Konstanten von heterogenen Substanzen, I-Dielektrizitätskonstanten und Leitfähigkeiten der Mischkörper aus isotropen Substanzen, *Annalen der Physik, Leipzig* 24 (1935) 636–679.
- [27] S.K. Das, S.U.S. Choi, W. Yu, T. Pradeep, *Nanofluids: Science and Technology*, John Wiley & Sons, Inc., Publication, New Jersey, the United States, 2008.
- [28] L.Q. Wang, X.S. Zhou, X.H. Wei, *Heat Conduction Mathematical Models and Analytical Solutions*, Springer-Verlag, Berlin, 2008.
- [29] P. Keblinski, S.R. Phillpot, S.U.S. Choi, J.A. Eastman, Mechanisms of heat flow in suspensions of nanosized particles (nanofluids), *Int. J. Heat Mass Transfer* 45 (2002) 855–863.
- [30] Y. Feng, A New Thermal Conductivity Model for Nanofluids with Convection Heat Transfer Application, MS Thesis, MAE Department, NC State University, Raleigh, NC, 2009.
- [31] S.P. Jang, S.U.S. Choi, Role of Brownian motion in the enhanced thermal conductivity of nanofluids, *Appl. Phys. Lett.* 84 (2004) 4316–4318.
- [32] D.H. Kumar, H.E. Patel, V.R.R. Kumar, T. Sundararajan, T. Pradeep, S.K. Das, Model for heat conduction in nanofluids, *Phys. Rev. Lett.* 93 (2004) 144301-1–144301-4.
- [33] J. Koo, C. Kleinstreuer, A new thermal conductivity model for nanofluids, *J. Nanopart. Res.* 6 (2004) 577–588.
- [34] J. Li, *Computational Analysis of Nanofluid Flow in Microchannels with Applications to Micro-heat Sinks and Bio-MEMS*, PhD Thesis, NC State University, Raleigh, NC, United States, 2008.
- [35] Y. Bao, Thermal conductivity equations based on Brownian motion in suspensions of nanoparticles (nanofluids), *J. Heat Transfer* 130 (2009) 042408-1–042408-5.
- [36] C. Kleinstreuer, Y. Feng, Thermal nanofluid property model with application to nanofluid flow in a parallel-disk system Part I: a new thermal conductivity model for nanofluid flow, *ASME J. Heat Transfer* (submitted for publication).
- [37] G. Roy, S.J. Palm, C.T. Nguyen, Heat transfer and fluid flow of nanofluids in laminar radial flow cooling systems, *J. Therm. Sci.* 14 (4) (2005) 362–367.
- [38] I. Gherasim, G. Roy, C.T. Nguyen, D. Vo-Ngoc, Experimental investigation of nanofluids in confined laminar radial flows, *Int. J. Therm. Sci.* 48 (2009) 1486–1493.
- [39] J.H. McGinn, Observations on the radial flow of water between fixed parallel plates, *Appl. Sci. Res. A* 5 (1956) 255–264.
- [40] M. Achintya, Analytical solutions of Nusselt number for thermally developing radial flow through small gap between two parallel disks, *J. Heat Transfer* 131 (2009) 054502-1–054502-4.
- [41] Y. Feng, C. Kleinstreuer, Thermal nanofluid property model with application to nanofluid flow in a microchannel Part II: nanofluid flow in a radial parallel-disk system, *ASME J. Heat Transfer*, (submitted for publication).
- [42] J.M. Li, Z.L. Li, B.X. Wang, Experimental viscosity measurements for copper oxide nanoparticle suspensions, *Tsinghua Sci. Tech.* 7 (2002) 198.